The Astronomical Journal, 168:139 (13pp), 2024 September https://doi.org/10.3847/1538-3881/ad6262

The Galactic Bulge Exploration. III. Calcium Triplet Metallicities for RR Lyrae Stars

Andrea Kunder[1], Zdenek Prudil[2], Claire Skaggs[1], Henrique Reggiani[3], David M. Nataf[4], Joanne Hughes[5], Kevin R. Covey[6], and Kathryn Devine[7]
[1] Saint Martin's University, 5000 Abbey Way SE, Lacey, WA 98503, USA
[2] European Southern Observatory, Karl-Schwarzschild-Strasse 2, 85748 Garching bei München, Germany
[3] Gemini Observatory/NSF's NOIRLab, Casilla 603, La Serena, Chile
[4] Department of Physics & Astronomy, The Johns Hopkins University, Baltimore, MD 21218, USA
[5] Physics Department Seattle University, 901 12th Ave., Seattle, WA 98122, USA
[6] Department of Physics & Astronomy, Western Washington University, MS-9164, 516 High St., Bellingham, WA 98225, USA
[7] The College of Idaho, 2112 Cleveland Blvd., Caldwell, ID 83605, USA
Received 2024 April 29; revised 2024 June 27; accepted 2024 July 1; published 2024 September 2

Abstract

RR Lyrae stars (RRLs) are excellent tracers of stellar populations for old, metal-poor components in the the Milky Way and the Local Group. Their luminosities have a metallicity dependence, but determining spectroscopic [Fe/H] metallicities for RRLs, especially at distances outside the solar neighborhood, is challenging. Using 40 RRLs with metallicities derived from both Fe(II) and Fe(I) abundances, we verify the calibration between the [Fe/H] of RRLs from the calcium triplet. Our calibration is applied to all RRLs with Gaia Radial Velocity Spectrometer (RVS) spectra in Gaia DR3 and to 80 stars in the inner Galaxy from the BRAVA-RR survey. The coadded Gaia RVS RRL spectra provide RRL metallicities with an uncertainty of 0.25 dex, which is a factor of two improvement over the Gaia photometric RRL metallicities. Within our Galactic bulge RRL sample, we find a dominant fraction with low energies without a prominent rotating component. Due to the large fraction of such stars, we interpret these stars as belonging to the in situ metal-poor Galactic bulge component, although we cannot rule out that a fraction of these belong to an ancient accretion event such as Kraken/Heracles.

Unified Astronomy Thesaurus concepts: Stellar populations (1622); RR Lyrae variable stars (1410); Distance indicators (394); Distance measure (395); Metallicity (1031); Gaia (2360); Galactic bulge (2041); Milky Way Galaxy (1054); Spectroscopy (1558); Infrared spectroscopy (2285)

Materials only available in the online version of record: machine-readable tables

1. Introduction

RR Lyrae stars (RRLs) are some of the few objects for which distances can be reliably inferred. They were the first stars that provided a distance to the center of the Galaxy, a fundamental parameter of the Milky Way (MW; Blanco & Blanco 1984), they are used to probe the most distant stars known in the MW halo (e.g., Medina et al. 2024; Feng et al. 2024), and their presence is used to find new low-luminosity globular clusters (GCs), substructures, and streams (e.g., Sesar et al. 2017; Prudil et al. 2021; Cook et al. 2022; Butler et al. 2024). RRLs are stars residing on the horizontal branch (HB), undergoing core helium burning. Because they reside on the part of the HB that intersects with the Cepheids' instability strip, they pulsate (radially). Their well-known pulsation cycle, with periods that range from ∼0.2 to 1.0 days and with pulsation amplitudes of ∼1 mag in optical passbands, ensures that they can be distinguished from other stars.

Pulsation properties of stars on the main instability strip are linked to their physical parameters, such as their luminosity and metallic content. Period–luminosity relations of RRLs are therefore often used to determine distances to the star. That the absolute magnitude is a function of the [Fe/H] metallicity for the V passband has been seen in stellar pulsation models (e.g., Christy 1966; Marconi et al. 2015), in stellar evolution tracks (Sweigart & Gross 1978; Demarque et al. 2000), and also in observational studies (e.g., Liu & Janes 1990; Cacciari et al. 1992; Carney et al. 1992; Fernley 1993; Sandage 1993; McNamara 1997; Fernley et al. 1998; Muraveva et al. 2018). In general, only [Fe/H] metallicity is taken into account when determining an RRL absolute magnitude (M_V) using optical passbands (e.g., Catelan et al. 2004).

In contrast to optical passbands, RRL absolute magnitudes in infrared (IR) passbands have been shown to be more affected by the pulsational period of the RRLs than their metallicity (e.g., Longmore et al. 1986; Catelan et al. 2004; Dall'Ora et al. 2004; Prudil et al. 2024a). Further, both theoretical models and observational studies show that the period–luminosity (PL) relations have a decreased scatter with increasing wavelength (e.g., Bono et al. 2003; Madore & Freedman 2012; Marconi et al. 2015; Vivas et al. 2017). But even with the longer passbands, incorporating a metallicity term in the RRL PL relations improves the derived distance precision by at least 1%–2% (e.g., Neeley et al. 2019; Muhie et al. 2021).

Photometric observations of RRLs allow periods to be determined with high accuracies, especially since most of the pulsation cycle of an RRL can typically be monitored over 12–18 hr. Unfortunately, this is not the case for the [Fe/H] metallicity of an RRL, and typically the main source of uncertainty when using RRLs to obtain distances is the metallicity component in the period–luminosity–metallicity (PLZ) relation. Exceptions to this are when it is reasonable to assume a single metallicity for the old stellar component, such as for cluster RRLs or for RRLs belonging to dwarf spheroidal

galaxies or ultrafaint dwarf galaxies, and metallicities from, e.g., red giants' spectra can be adopted. The three main methods to determine RRL metallicities are from high-resolution spectroscopy, from low-resolution spectroscopy, and/or from the shape of the RRLs' photometric light curve.

High-resolution spectroscopy ($R \gtrsim 25{,}000$) provides a direct measurement of the metallicity of an RRL, often with the highest accuracy and smallest [Fe/H] uncertainty compared to the other methods mentioned above. Unfortunately, high-resolution spectroscopy is typically feasible only for RRLs within a few kiloparsecs from the Sun, as RRL absolute magnitudes ($M_V \sim 0.7$) make spectroscopic observations of RRLs in the Galactic bulge and beyond both challenging and resource intensive. There are ∼180 RRLs with metallicities determined from high-resolution spectroscopy (e.g., Dambis et al. 2013; Liu et al. 2013; Fabrizio et al. 2019; Gilligan et al. 2021; Crestani et al. 2021a). These abundances are on the Chadid et al. (2017), For et al. (2011), Crestani et al. (2021a), and Sneden et al. (2017) metallicity scale (abbreviated CFCS). In order to probe metallicities for RRLs in the outer halo of the MW, in the Galactic bulge, or in external galaxies, lower-resolution spectroscopy or photometric metallicities, $[Fe/H]_{phot}$, need to be employed.

Lower-resolution spectroscopy relies mainly on the ΔS method to obtain a [Fe/H] metallicity (e.g., Preston 1959; Clementini et al. 1991). This method consists of comparing the spectral type or equivalent widths (EWs) of the RRL using one family of lines (e.g., the hydrogen lines, Hβ, Hγ, Hδ) to the spectral type or EW of the RRL using a different line (e.g., the Ca ii K line). These hydrogen and calcium lines are strong and dominate the spectrum, making them straightforward to identify and use as tracers of [Fe/H] metallicity. This ΔS—the difference between the spectral type or EWs from different spectral lines—is directly correlated with the [Fe/H] metallicity of an RRL (e.g., Butler 1975; Butler et al. 1982; Walker & Terndrup 1991; Layden 1994). Wallerstein et al. (2012) showed that the ΔS method can be used with only the EW of the Ca ii line at 8498 Å to derive an RRL [Fe/H] metallicity. This is especially useful if the wavelength regime is insufficient to cover both Ca ii lines and Hβ, Hγ, Hδ lines.

The use of photometric metallicities for RRLs relies on an empirical relation between mathematical coefficients that measure the RRL light-curve shape, the period, and the [Fe/H] metallicity. An RRL light-curve shape is frequently quantified by a Fourier decomposition to the RRL's periodic photometric signal (Jurcsik & Kovacs 1996), but other mathematical coefficients that describe the shape of the RRL's light curve have also been used (e.g., using a principal component analysis; Kanbur & Mariani 2004). A recent study utilizing the Crestani et al. (2021a) high-resolution metallicities, combined with thousands of lower-resolution metallicities from LAMOST DR6 and SDSS-SEGUE, shows that the intrinsic scatter in the photometric metallicities is 0.41 dex in the V band and 0.50 dex in the IR (Mullen et al. 2021).

Here we focus on using lower-resolution spectroscopy covering the Ca ii lines to probe the [Fe/H] metallicities of RRLs, $[Fe/H]_{CaT}$. The calcium lines were first used as metallicity indicators because the Ca ii IR triplet is red enough to reduce the effect of interstellar extinction and hence to allow heavily reddened clusters in the MW to be spectroscopically analyzed (e. g., Armandroff & Zinn 1988). Since then, the use of Ca ii lines to measure metallicity has especially shown to be powerful for metal-poor stars (e.g., Starkenburg et al. 2010; Carrera et al. 2013; Matijevič et al. 2017), as for low-metallicity stars ($[Fe/H] < -2.0$) many metallic lines become almost indistinguishable from the background noise, but the Ca ii lines are still prominent.

The calibration of the EW of the 8498 Å Ca ii line in RRLs to [Fe/H] metallicity was first presented by Wallerstein et al. (2012), with the goal of using this calibration to derive metallicities of RRLs that would be observed by Gaia. Only the 8498 Å Ca ii line was used, as the others were often blended by neighboring hydrogen Paschen lines. The calibrating sample is based on $R \sim 35{,}000$ spectra from the Apache Point Observatory echelle spectrograph of ∼30 RRLs. This relation has been applied to 935 RRLs in the Galactic bulge observed in the Bulge Radial Velocity Assay for RR Lyrae stars (BRAVA-RR) survey (Kunder et al. 2016, 2020) to obtain the first spectroscopic metallicity distribution function for a large sample of RRLs in the Galactic bulge (Savino et al. 2020). The global metallicity distribution function was shown to be good to 0.35 dex, but individual RRL $[Fe/H]_{CaT}$ metallicities could have much larger uncertainties, hampered mainly by the low signal-to-noise ratio (S/N) of the BRAVA-RR spectra.

Ca ii abundances have not been applied to the Gaia RRLs yet, but this has tremendous potential considering the plethora of Gaia spectra that are, or will be, available with ongoing Gaia data releases. There also exists the possibility to obtain $[Fe/H]_{CaT}$ for individual BRAVA-RR stars with uncertainties that allow for a chemodynamical mapping of the stellar population in the inner Galaxy. In Section 2 we expand on the Wallerstein et al. (2012) EW−[Fe/H] calibration and verify its accuracy. $[Fe/H]_{CaT}$ abundances for 175 Gaia RRLs are obtained and discussed in Section 3, and an analysis of how α affects the Gaia photometric metallicities, $[Fe/H]_{phot,DR3}$, of a star is carried out. $[Fe/H]_{CaT}$ metallicities of 80 Galactic bulge RRLs are derived in Section 4 and used to probe the signature of the earliest known MW accretion event, Heracles. Our conclusions are provided in Section 5.

2. Calibration of the Calcium Triplet

Here we carry out an independent study from that by Wallerstein et al. (2012) to probe the dependence of the EW of the 8498 Å Ca ii line in RRLs on their [Fe/H] metallicity. Fundamental-mode RRLs (RRab), first-overtone RRLs (RRc), and double-mode pulsators (RRd) with spectroscopic [Fe/H] abundances and photometric (pulsation properties) information are available in Crestani et al. (2021a), and this sample was used as calibrators of the Ca ii–[Fe/H] relation. The ESO archive[8] was used to access the RRL spectra from the UVES ($R \approx 40{,}000$) and XSHOOTER ($R \approx 10{,}000$) instruments. Additionally, spectra from the RAVE survey ($R \approx 7500$; Steinmetz et al. 2020) were obtained for a handful of RRLs with [Fe/H] in the Crestani et al. (2021a) compilation. In total, 68 spectra for 40 single-mode pulsators were collected, and for each spectrum we obtained its S/N, resolution, exposure, and observation time. The S/N of the RRL spectra varied between 28 and 222, with a median centered at 69. The spectra collected are listed in Table 1, where the columns list (1) each RRL's Gaia ID, (2) [Fe/H] from Crestani et al. (2021a), (3) period, (4) time of maximum brightness, (5) time the spectra were taken, (6) type of single-mode RRL, (7) spectral name from archive,

[8] https://archive.eso.org/scienceportal/home

Table 1
RR Lyrae Star Spectra Used to Calibrate the EW for Ca ii at 8498 Å to [Fe/H] Metallicity

Gaia ID (1)	[Fe/H] (2)	Per (3)	M_0 (4)	HJD (5)	Type (6)	Name (7)	S/N (8)	Resolution (9)	Instrument (10)	EW (11)
6539269990871163392	-1.78 ± 0.11	0.6587047	2453694.233837	2457288.627074	RRab	ADP.2017-05-12T07:46:45.719	59	11333	XSHOOTER	577.1 ± 19.8
6677541412082758144	-2.39 ± 0.11	0.4069942	2454330.624998	2457288.547716	RRc	ADP.2017-05-12T07:46:45.749	41	11333	XSHOOTER	419.6 ± 12.5
6483680332235888896	-1.62 ± 0.01	0.4795935	2457223.412508	2457618.643778	RRab	ADP.2017-05-12T15:04:34.079	163	18340	XSHOOTER	638.5 ± 3.8
4918030715504071296	-1.68 ± 0.14	0.3332324	2456833.506586	2454050.972451	RRc	20061111_0005m59_080	36	7500	RAVE	592.2 ± 22.9
3806559592377384704	-1.64 ± 0.14	0.4631965	2457128.057598	2457782.714295	RRab	ADP.2017-05-12T19:12:51.203	51	8935	XSHOOTER	541.7 ± 10.5
2608819623000543744	-2.31 ± 0.04	0.608874	2457593.585532	2457234.761289	RRab	ADP.2020-06-10T17:26:03.411	68	42310	UVES	524.9 ± 3.0

Note.[*]The full version of this table is available in machine-readable format in the online journal. A portion is shown here for guidance regarding its form and function.

(This table is available in its entirety in machine-readable form in the online article.)

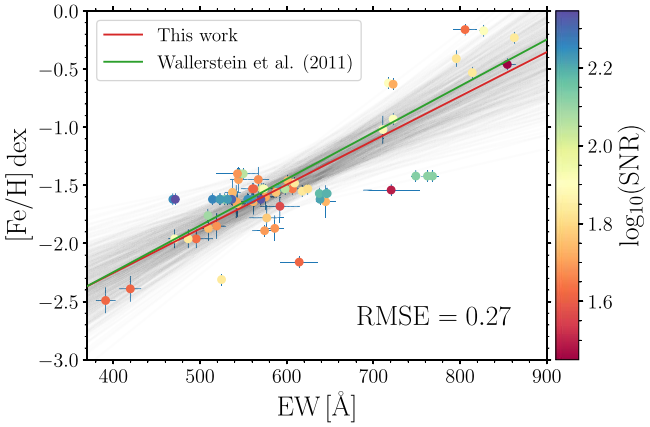

Figure 1. The calibrated linear relation (red line) between spectroscopic [Fe/H] and EW of the Ca ii line at 8498 Å. The color-coding illustrates the S/N of the individual measurements. The individual measurements with all their available measurements are shown, so some individual RRLs are represented here repeatedly. The green line represents the calibration relation from Wallerstein et al. (2012).

(8) S/N, (9) resolution, (10) instrument, and (11) measured EW and uncertainty about the measurement.

To estimate EWs for Ca ii at 8498 Å from each spectrum, a Python routine was developed that allows the user to select continuum and line regions based on the properties of individual spectra in order to measure the EWs for Ca ii at 8498 Å from each spectrum (see example fit for Gaia Radial Velocity Spectrometer (RVS) spectra in Figure 3). The routine works with a pre-synthesized spectrum using the iSpec module (Blanco-Cuaresma et al. 2014; Blanco-Cuaresma 2019) for typical RRLs ([Fe/H] = −1.5 dex, $T_{\rm eff}$ = 6500 K, log g = 2 dex) that serves as a guide to locate continuum regions in the spectrum. As in Wallerstein et al. (2012), only the EWs for the Ca ii lines at 8498 Å were measured, as this line is the farthest from the hydrogen line of the Paschen series.

Figure 1 shows the correlation between our measured EWs for Ca ii at 8498 Å and the [Fe/H] metallicities from Crestani et al. (2021a). Both our measured EWs and the [Fe/H] abundances were derived with their associated uncertainties, so our fitting procedure considers both sources of error when determining the best relation between the two. Because both of these quantities were derived independently, we assume that the correlation between them is negligible. The utilized covariance matrix Ξ^i for a given star (i) has the following form:

$$\Xi^i = \begin{bmatrix} \sigma^i_{\rm EW} & 0 \\ 0 & \sigma^i_{\rm [Fe/H]} \end{bmatrix}. \quad (1)$$

To obtain the best fit, the procedure by Hogg & Bovy (2010, see their Section 7) was followed, an approach that is fairly similar to the orthogonal least-squares method. In this method, the slope of the linear relation a is described by a unit vector $\boldsymbol{v}$ perpendicular to the linear fit:

$$\mathbf{v} = \frac{1}{\sqrt{1+a^2}} \begin{bmatrix} -a \\ 1 \end{bmatrix}. \quad (2)$$

The slope is defined by an angle θ via $a = \tan(\theta)$. Each data point i (EW^i and [Fe/H]^i) can be represented by a vector $\boldsymbol{Z}_i$ = (EW^i, [Fe/H]^i). The orthogonal displacement δ_i for each point is then

$$\delta_i = \boldsymbol{v}^{\rm T} \times \boldsymbol{Z}_i - b \cdot \cos(\theta), \quad (3)$$

where the parameter b represents the intercept of the linear fit. In addition to the slope and intercept, we included ε, representing the intrinsic scatter in the EW versus [Fe/H] relation. The orthogonal variance Σ^2_i is then described by

$$\Sigma^2_i = \boldsymbol{v}^{\rm T} \times \Xi_i \times \boldsymbol{v} + \exp\varepsilon. \quad (4)$$

The aforementioned parameters then form the following relation for the log-likelihood function ln(p):

$$\ln(p) = K \sum_i^N \frac{\delta_i^2}{2\Sigma_i^2}, \quad (5)$$

where K is a constant. The log-likelihood function can be optimized for the linear model parameters a and b, yielding the best values for a, b, and ε. In the maximization of the log-likelihood, we utilized the emcee module (Foreman-Mackey et al. 2013), and we ran the Markov Chain Monte Carlo simulation with 200 walkers for 10,000 samples. For deriving the best-fit values, we thinned the sample by $\tau = 100$ and marked the initial 5000 samples as burn-in.

In this way, the following relation and covariance matrix were obtained:

$$[{\rm Fe/H}]_{\rm CaII} = 0.0038 \cdot {\rm EW} - 3.77$$
$$\rm Cov = \begin{bmatrix} 0.0000014 & -0.0008481 \\ -0.0008481 & 0.5160122 \end{bmatrix} \qquad \varepsilon = 0.04. \quad (6)$$

This relation has an rms error (RMSE) of 0.27 dex and is remarkably similar to that presented in Wallerstein et al. (2012). Although our relation was derived using RRab, RRc, and RRd pulsators, there are more RRab-type RRLs in our calibration sample than RRc or RRd stars, so the calibration is most appropriate for RRab stars. We examined how the quality of the spectra, as represented by the S/N, influenced our calibration by applying several S/N cuts. The resulting relation in Equation (6) does not exhibit significant changes within the 1σ errors listed in its covariance matrix. Overall, the quality of the selected spectra is high and has a negligible influence on the final calibration. Because all of our calibration RRLs are from the Crestani et al. (2021a) sample, this calibration is on the CFCS metallicity scale.

3. Gaia RR Lyrae Star Metallicities

Individual photometric metallicities for Gaia RRLs presented in Gaia DR3 come from the Specific Object Study (SOS) pipeline. The SOS module that provides the community with photometric [Fe/H] metallicities uses the RRL pulsation period, P, and the ϕ_{31}[9] parameters of the G light-curve Fourier decomposition with the equation derived in Nemec et al. (2013):

$$[{\rm Fe/H}]_{\rm phot,DR3} = -5.241 - 5.394P + 1.345\,\phi_{31}. \quad (7)$$

In this way, metallicities are available for 133 557 RRLs in the Gaia data archive. Clementini et al. (2023) validate these photometric metallicities by comparing with the high-

[9] $\phi_{31} = \phi_3 - 3\phi_1$, where ϕ_k are Fourier phases from a sine-series sum: $m(t) = A_0 + \sum_{k=1}^{N} A_k \sin(k2\pi t/P + \phi_k)$.

Table 2
Gaia Photometric [Fe/H] Metallicity Relations

Authors (1)	Photometric [Fe/H] Relation (2)	$\sigma_{\rm published}$ (3)	$\sigma_{\rm CaT,\ All\ S/N}$ (4)	$\sigma_{\rm CaT,\ S/N>35}$ (5)	Correlation in [α/Fe] (6)
Clementini et al. (2023)	RRab: −5.241 −5.394 P + 1.345 ϕ_{31}	0.46	0.52	0.44	−0.74 ± 0.32
	RRc: −5.241 −5.394 P + 1.345 ϕ_{31}	0.46	0.44	0.37	
Iorio & Belokurov (2021)	RRab: −1.68 −5.08 (P-0.6) + 0.68 (ϕ_{31}-2.0)	0.31	0.34	0.22	−1.43 ± 0.18
	RRc: −1.26 −9.39 (P-0.3) + 0.29 (ϕ_{31}-3.5)	0.16	0.37	0.34	
Li et al. (2023)	RRab: −1.888 −5.772 (P-0.6) + 1.09 (ϕ_{31}-2.0) + 1.065 (R21-0.45)	0.24	0.36	0.22	−0.95 ± 0.22
	RRc: −1.737 −9.968 (P-0.3) + -5.041 (R21-0.2)	0.19	0.33	0.31	
Dékány & Grebel (2022)	RRab: Neural Network	0.21	0.42	0.26	−0.81 ± 0.17
Jurcsik & Hajdu (2023)	RRab: −3.504 + 3.14 −5.716 P + 1.019 ϕ_{31}	0.21	0.43	0.20	−1.04 ± 0.21
This Work	RRab: −5.5061 P + 0.8143 ϕ_{31} - 0.0813	0.25	0.35	0.21	−0.95 ± 0.19
	RRc: −13.2023 P + 0.5138 ϕ_{31} + 0.7338	0.19	0.44	0.40	

resolution metallicities of Crestani et al. (2021a). They find a mean photometric metallicity error of 0.46 dex.

The Gaia all-sky RRL catalogs have also generated interest in developing photometric metallicities in the G band (Iorio & Belokurov 2021; Li et al. 2023; Dékány & Grebel 2022; Jurcsik & Hajdu 2023; Clementini et al. 2023). None of the photometric metallicity relations put forward to date, however, use the large, homogeneous spectroscopic survey of field RRLs from Crestani et al. (2021a), which covers more than 3 dex in iron abundance, as a calibrating sample. We believe that this sample has a great potential to anchor a photometric metallicity calibration in both the metal-poor and metal-rich ends of the RRLs and that the homogeneity of the analysis of this sample can reduce effects of intrinsic scatter in the calibrating sample. Therefore, a calibration of the photometric metallicity using the Gaia G passband is carried out for both RRab and RRc stars using the Crestani et al. (2021a) stars as calibrators. These results can be found in the Appendix and are summarized in Table 2.

Table 2 also summarizes additional relations put forward for photometric [Fe/H] metallicities from previous studies. Iorio & Belokurov (2021) use 84 RRLs from the spectroscopic sample of Layden (1994) to calibrate a photometric [Fe/H] for RRLs with an intrinsic scatter of 0.31 dex for the RRab stars and 0.16 dex for RRc stars. Li et al. (2023) use a catalog of ∼5290 RRLs from Liu et al. (2020) to calibrate $[{\rm Fe/H}]_{\rm phot}$ using the Gaia photometric properties of their observed RRLs. They find a scatter of 0.24 dex for their RRab relation and 0.19 dex for their RRc relation. Dékány & Grebel (2022) use deep learning and the Gaia G-band light curves that have a near-IR K_s-band light-curve counterpart to train a neural network for a $[{\rm Fe/H}]_{\rm phot}$ estimation. The results from this process were then applied to other passbands, such as the Gaia G band, and were found to have a scatter comparable to the Crestani et al. (2021a) high-resolution uncertainties. Jurcsik & Hajdu (2023) use the Gaia G-band RRL light curves that overlap with a GC RRL to assemble a sample of 526 high-quality RRLs belonging to 70 GCs. The high-resolution, well-studied spectroscopic [Fe/H] metallicities of the GCs are used as calibration $[{\rm Fe/H}]_{\rm phot}$ metallicities. They find that their relation does not work for Oosterhoff II−type RRLs—RRLs with longer periods for their pulsation amplitudes—and they do not believe that there is a photometric [Fe/H] relation that is accurate for Oosterhoff II RRLs. Note that local RRLs in general are Oosterhoff I−type RRLs; it is the more metal-poor RRLs that tend to be Oosterhoff II−type stars (e.g., Prudil et al. 2019, 2020).

3.1. RRL Photometric Metallicities Compared to Calcium Triplet Metallicities

The brighter stars observed by the Gaia satellite ($G \sim 16$) have medium-resolution spectra delivered by RVS ([845–872] nm, $\lambda/\Delta\lambda \sim 1500$). In the current Gaia data release, DR3, there are 213 Gaia RRLs with RVS spectra available for download (`gaia_source.has_rvs=true`). However, 36 of those have no clean RV epochs (`num_clean_epochs_rv = "null''`) and correspondingly have no average radial velocity; these are not used in our analysis. Therefore, our final Gaia RRL RVS sample consists of 177 stars. Only coadded spectra are available for download, and therefore the Gaia spectra contain contributions from all the observed phases of the RRL in their Ca lines. Whereas a discussion on how the EW of the CaT changes as a function of phase cannot be carried out using the Gaia RVS spectra, we are able to use single-epoch spectra from the BRAVA-RR survey to examine the effect of pulsation phase on $[{\rm Fe/H}]_{\rm CaT}$, and this is discussed in Section 4.

The number of spectra stacked to make the mean Gaia RVS spectra ranges from 7 to 54 coadded exposures, and the S/N of the spectra ranges from 20 to more than 80 for the brightest RRLs. The top right panel of Figure 3 shows an example of the coadded RVS spectra of a sample of Gaia RRLs with different S/Ns.

The dispersion between our $[{\rm Fe/H}]_{\rm CaT}$ metallicities and the published photometric metallicities is reported in Table 2, and Figure 2 shows the difference between our $[{\rm Fe/H}]_{\rm CaT}$ metallicities and the photometric metallicity relations. A total of 137 RRLs can be compared, as 38 RRLs with RVS spectra do not have light curves with sufficient Gaia photometric measurements for a ϕ_{31} value (and hence do not have a photometric [Fe/H] metallicity) and 2 RRLs did not have spectra that enabled a robust EW measurement. The Dékány & Grebel (2022) and Jurcsik & Hajdu (2023) photometric metallicities are only derived for RRab stars, and so only the 100 RRab stars are shown. The photometric metallicity relation presented here (Appendix) and those from Iorio & Belokurov (2021), Li et al. (2023), and Clementini et al. (2023) are given

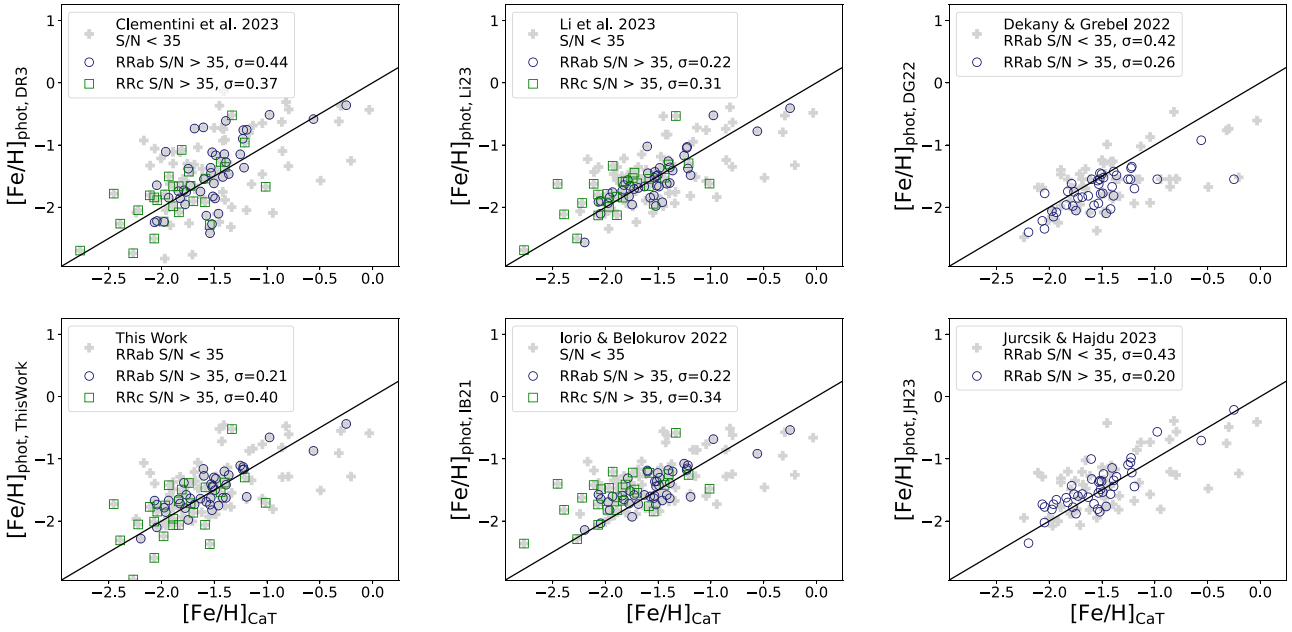

Figure 2. The difference between the [Fe/H] metallicity determined from the 8498 Å Ca II line and the [Fe/H] metallicity determined from different photometric *G*-band light-curve−metallicity relationships in the literature. The dispersion for the RRLs with RVS spectra with S/N > 35 and S/N < 35 is indicated in each panel. Our CaT metallicities have dispersions comparable to the precision of the photometric [Fe/H] metallicities for RRLs with S/N > 35. The bottom left panel shows the photometric metallicity from this study; the calibration is described in the Appendix.

for both RRab and RRc stars, and so 100 RRab and 37 RRc stars are displayed.

Here it is evident that $[Fe/H]_{CaT}$ is a function of both S/N and pulsation mode (e.g., RRab or RRc). $[Fe/H]_{CaT}$ metallicities agree better with photometric metallicities for those stars with higher-S/N spectra, and also for RRab stars rather than for RRc stars. The dispersion between $[Fe/H]_{phot}$ and $[Fe/H]_{CaT}$ is given for both the RRab and RRc stars with RVS spectra with S/N > 35.

The dispersion between $[Fe/H]_{phot,DR3}$ and $[Fe/H]_{CaT}$ is $\sigma = 0.41$ for the 70 stars with S/N > 35, which is comparable to the mean photometric metallicity error. In contrast, the dispersion between the photometric and CaT [Fe/H] metallicities is $\sigma = 0.52$ for the 65 stars with S/N < 35. The scatter between $[Fe/H]_{CaT}$ and the independent $[Fe/H]_{phot}$ values shows an improved agreement as compared to $[Fe/H]_{phot,GaiaDR3}$, indicating that the uncertainty in our $[Fe/H]_{CaT}$ metallicities is at least comparable to $[Fe/H]_{phot}$ for spectra with S/N > 35. The uncertainties in $[Fe/H]_{CaT}$ are further assessed using comparisons with high-resolution spectra below.

3.2. Gaia Metallicities Compared to High-resolution Metallicities

Twenty-two members of our Gaia RRL RVS sample were observed by Crestani et al. (2021a) in their high-resolution spectroscopy sample. The dispersion between the Crestani et al. (2021a) metallicities and those obtained from the CaT is $\sigma = 0.30$ for the full sample and $\sigma = 0.25$ for the RVS spectra with S/N > 35, as seen in Figure 3. Because the Crestani et al. (2021a) compilation also includes Ca, Ti, and Mg elemental abundances, how α-abundances affect $[Fe/H]_{CaT}$ can be investigated. The right panel of Figure 3 does not show any indication that $[\alpha/Fe]$ affects the derived $[Fe/H]_{CaT}$, but this is still a small sample. It is further possible to use the Crestani et al. (2021a) α-abundances to investigate how α affects the Gaia photometric metallicities. In this case the sample size will be larger, as $[Fe/H]_{phot}$ is independent of the available RVS spectra.

Figure 4 shows how $[Fe/H]_{phot}$ from different relations correlate with $[\alpha/Fe]$, where $\Delta[Fe/H]_{phot,DR3}$ corresponds to $[Fe/H]_{CaT} - [Fe/H]_{phot,DR3}$. There is a trend between $\Delta[Fe/H]_{phot,DR3}$ and $[\alpha/Fe]$ for all the photometric metallicity relationships. If a linear relation is adopted, all relations show a significant slope, reported in the legend for each panel and in Table 2. In all cases, the photometric metallicities tend to underpredict [Fe/H] for RRLs depleted in $[\alpha/Fe]$ and overpredict the metallicity of RRLs enhanced in $[\alpha/Fe]$. That the α-abundance affects $[Fe/H]_{phot}$ is not surprising, as RRLs are often enhanced in α but depleted in [Fe/H]. Therefore, it is not inconceivable that α plays a significant role in the shape of the RRL light curve, which is what ϕ_{31} measures. One of the advantages of $[Fe/H]_{CaT}$ is that there does not appear to be the same kinds of biases with $[\alpha/Fe]$ abundance that are present in metallicities derived from photometry. The difference between $[Fe/H]_{CaT}$ and $[Fe/H]_{phot}$ may also indicate the $[\alpha/Fe]$ of a star. RRLs with $\Delta[Fe/H] > 0.3$ are likely to have low $[\alpha/Fe]$ abundances.

We list in Table 3 CaT metallicities derived for the Gaia RRLs with RVS spectra. Only a small portion of the table is shown here for clarity; the full table is available online.

4. Calcium Triplet Metallicities of BRAVA-RR RRLs

The BRAVA-RR survey is a spectroscopic survey targeting RRLs in the inner Galaxy (Kunder et al. 2016, 2020). To date ∼2700 RRLs have been observed using AAOmega on the Anglo-Australian Telescope with a similar resolution and wavelength regime to Gaia. The BRAVA-RR results have shown that the RRLs in the inner Galaxy are not a homogeneous population; some follow the barred Galactic bulge, and some have properties that indicate that they formed before the bar. In particular, the most centrally concentrated

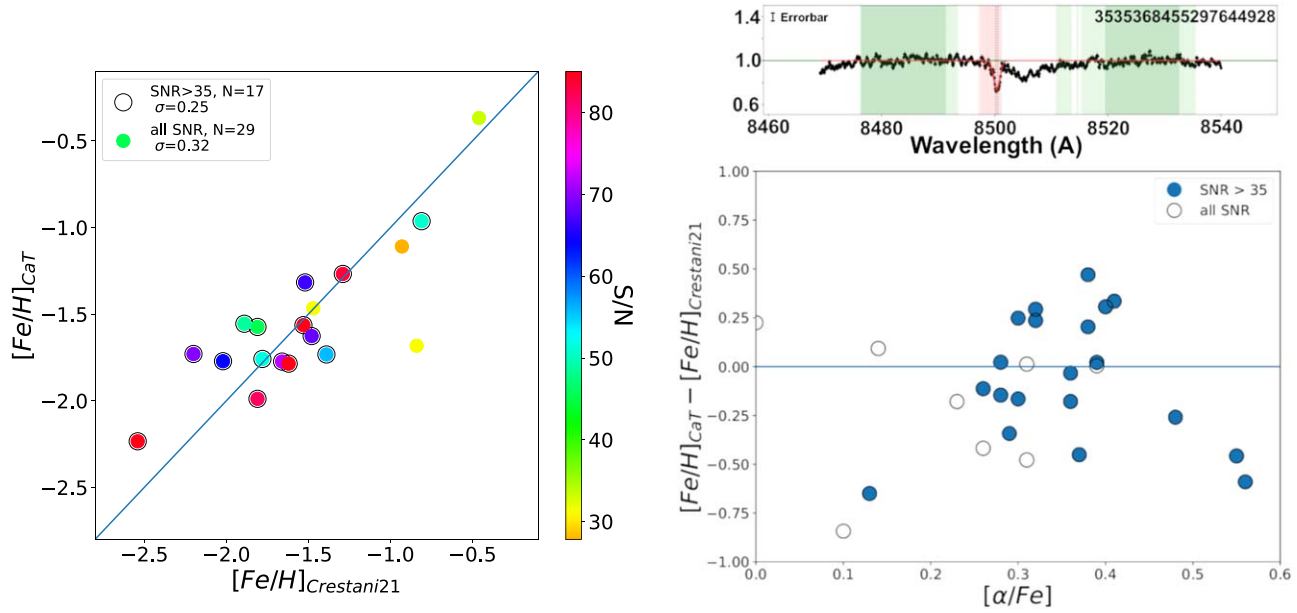

Figure 3. Left: the high-resolution [Fe/H] metallicities of Crestani et al. (2021a), $[Fe/H]_{Crestani21}$, compared to $[Fe/H]_{CaT}$ of the same stars. Bottom right: the [α/Fe] abundance as a function of the difference between $[Fe/H]_{CaT}$ and $[Fe/H]_{Crestani21}$. The $[Fe/H]_{CaT}$ calibration does not appear significantly affected by α, but the sample size is small. Top right: the Gaia coadded RVS spectra of RRLs with S/N $\sim$ 35. The blue and red continua of the spectra are manually selected (green regions), as is the position of the CaT line at 8498 Å, for which the EW is then measured.

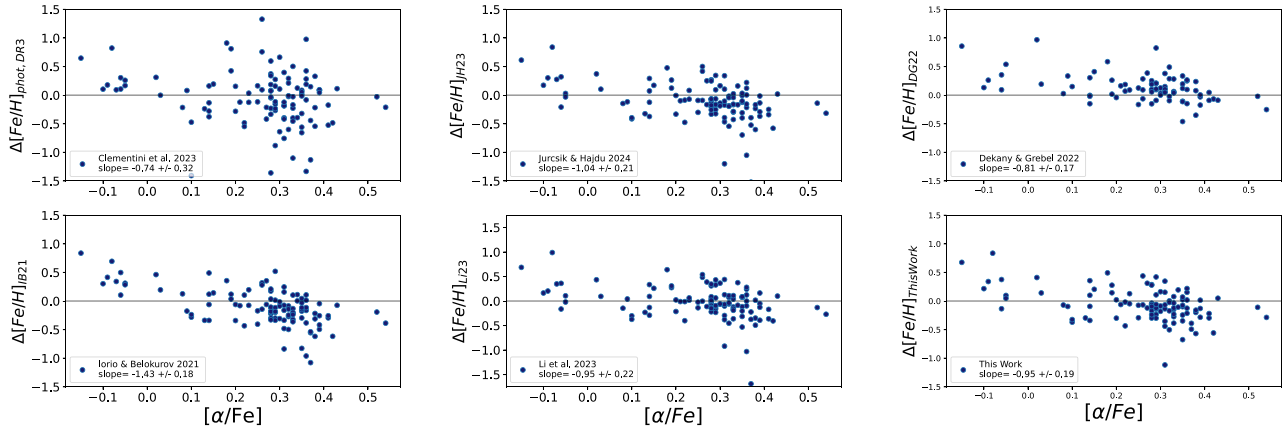

Figure 4. The [α/Fe] abundance as a function of the difference between $[Fe/H]_{CaT}$ and $[Fe/H]_{phot}$, where the different $[Fe/H]_{phot}$ relations of Clementini et al. (2023), Iorio & Belokurov (2021), Li et al. (2023), Dékány & Grebel (2022), Jurcsik & Hajdu (2023), and this study (Appendix) are compared. In all cases, $[Fe/H]_{phot}$ is a function of the α-enrichment of the RRL, with Δ[Fe/H] > 0.5 indicating a star with a low [α/Fe] abundance.

Table 3
The [Fe/H] Metallicities of Local RRLs from Gaia RVS Spectra Using the EW of the 8498 Å Ca ii Line

Gaia ID	R.A. (deg)	Decl. (deg)	EW	[Fe/H]	S/N	No. Clean Epochs	*G*-mag
(1)	(2)	(3)	(4)	(5)	(6)	(7)	(8)
1026974891482561792	129.357206	49.268806	512.69 ± 23.86	−1.82 ± 0.17	25	17	12.068
1032533743099023360	122.009609	53.658476	537.67 ± 23.07	−1.73 ± 0.17	27	21	12.299
1036978866747819264	132.811239	56.355288	554.42 ± 10.44	−1.66 ± 0.15	60	25	11.250
1050307829598059008	149.453252	60.741150	496.99 ± 31.49	−1.88 ± 0.18	29	50	13.131
1063808840251264128	146.736001	63.695459	659.17 ± 7.70	−1.27 ± 0.14	79	38	10.883
1093345639583902592	126.102594	65.717379	510.84 ± 7.29	−1.83 ± 0.14	75	26	11.000
1094115263363633408	127.130048	67.496421	405.13 ± 18.57	−2.23 ± 0.16	29	43	12.598
1104405489608579584	98.499256	67.025256	694.25 ± 34.98	−1.13 ± 0.19	24	33	12.799
1151084568571408384	125.681151	86.081024	490.75 ± 22.12	−1.91 ± 0.16	26	23	12.302

Note.[*]The full version of this table is available in machine-readable format in the online journal. A portion is shown here for guidance regarding its form and function. (This table is available in its entirety in machine-readable form in the online article.)

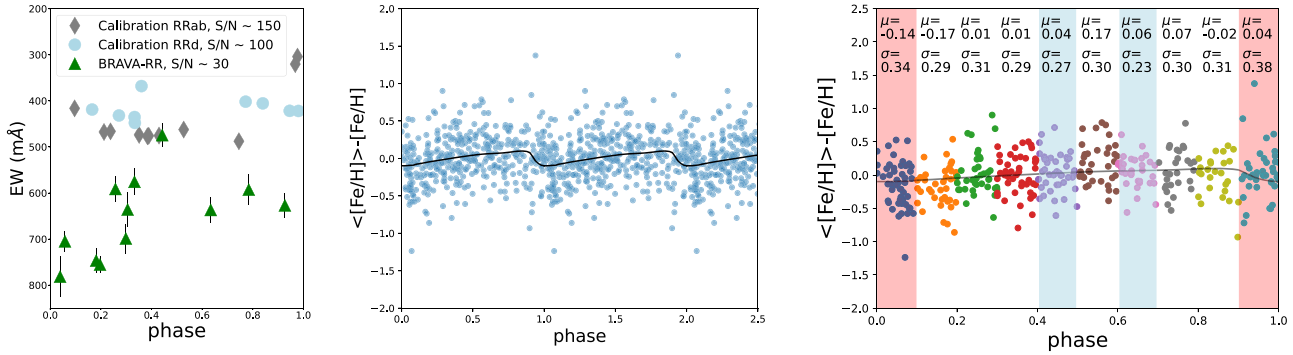

Figure 5. Left: an example of how the EW of an RRL changes with phase. Middle: the difference between each individual $[Fe/H]_{CaT}$ measurement as compared to the stars $\langle[Fe/H]_{CaT}\rangle$. The light curve of a type ab RRL is overplotted. Right: same as the middle panel, but only the scatter about each phase is reported. Phases with the largest scatter in $[Fe/H]_{CaT}$ are highlighted in red, and the optimal phases with low $[Fe/H]_{CaT}$ scatters are highlighted in blue.

RRLs have tight orbits with large eccentricities and a spatial distribution that does not show a clear barred distribution (see Figure 6 in Kunder et al. 2020). Whereas this population is elusive in most inner Galaxy studies targeting the more numerous metal-rich Galactic bulge stars (e.g., Queiroz et al. 2021), recent studies of metal-poor giants have confirmed an ancient, centrally concentrated stellar population that was part of the first few massive progenitors to form the proto-Galaxy (Belokurov & Kravtsov 2022; Ardern-Arentsen et al. 2024).

Accretion remnants will also reside in the inner Galaxy, and it is well-known that different progenitor populations lead to different loci in total energy versus angular momentum space (e.g., Massari et al. 2019). Das et al. (2020) also show that accreted structures can be identified from their Mg, Mn, and Fe abundances. In this way, the detections of the Gaia-Enceladus/Sausage system (GE/S; Belokurov et al. 2018; Helmi et al. 2018), the Splash accretion (Belokurov et al. 2020), and the inner Galaxy structure known as Heracles (Horta et al. 2021)[10] have been detected within the central ∼4 kpc of the Galaxy using bright giant stars.

Giants will span a wide range of ages, and this can dilute or introduce noise into the signature of old accreted systems. Selecting only stars with low metallicities can help cull the younger giants, but selecting stars by their age is difficult. RRLs, in contrast to giants, are exclusively an old population and are therefore useful to probe the first large accretion events in the Galaxy. None of the abovementioned accretion events have been seen within the inner Galaxy RRL population yet, although GE/S has been detected in the local RRL population (e.g., Prudil et al. 2020).

The lack of spectroscopic metallicities for the inner Galaxy RRLs makes it difficult to chemically link any dynamical properties of inner Galaxy RRLs to the accretion history of the MW. In particular, accreted stars will have depleted Mg abundances ($[Mg/Fe] < 0.2$) for stars more metal-rich than $[Fe/H] \sim -1.25$. The $[Fe/H]_{CaT}$ metallicities enable a search for stars that could be in the GE/S, Splash, or Heracles.

4.1. Use of Calcium Triplet [Fe/H] Abundances for Galactic Bulge RRLs

From the BRAVA-RR Survey, the 83 RRLs with more than eight epochs of observations were selected with which to determine $[Fe/H]_{CaT}$. The numerous epochs allow the investigation of the relationship between $[Fe/H]_{CaT}$ and phase to be investigated. In addition, multiple epochs can be averaged together for a more robust $[Fe/H]_{CaT}$ metallicity, which is helpful because the S/N for the BRAVA-RR spectra is typically ∼10–40.

The left panel of Figure 5 shows the measured EW as a function of phase for the star OGLE-BLG-RRLYR-10715, as well as for the two calibration stars with the highest number of epochs, the RRab star V Ind and the RRd star V5644 Sgr (see Table 1). The scatter in the measured EW with phase is more prominent in the low-S/N stars, and only minor scatter in EW is observed in spectra with high S/Ns.

In order to combine the full sample of RRLs and determine how the pulsation phase affects $[Fe/H]_{CaT}$, we first determine the mean $[Fe/H]_{CaT}$ from all of the stars' measurements, $\langle[Fe/H]_{CaT}\rangle$. Only spectra with S/N >25 are included in our analysis, which is 60% of the BRAVA-RR measurements for our sample of 83 RRLs. The middle panel of Figure 5 shows the difference between $\langle[Fe/H]_{CaT}\rangle$ and $[Fe/H]_{CaT}$ of 659 measurements for the 83 individual BRAVA-RRLs in our sample. The characteristic sawtooth shape of the RRL pulsations is seen, and the Liu (1991) template is overplotted.

The mean difference and scatter of the individual $[Fe/H]_{CaT}$ measurement for each phase can be calculated, and this is shown in the right panel of Figure 5. The mean difference in the individual $[Fe/H]_{CaT}$ measurement for each phase, μ, is in agreement that the systemic velocity (which can also be thought of as the zero-velocity phase, since this is the best approximation of a "static" star behavior) occurs at $\phi \sim 0.38$ (Liu 1991; Kunder et al. 2020; Prudil et al. 2024b).

It is not surprising that phases with $\phi > 0.9$ and $\phi < 0.1$ have the largest scatter; these phases are often reported to correspond to a shocked atmosphere phase (Pancino et al. 2015; Kolenberg et al. 2010) and also rapid changes in temperature (e.g., Preston et al. 2022) and hence are regions where the spectra may be affected by shocks. The phases with the smallest scatter are those between $\phi = 0.4$–0.5 and $\phi = 0.6$–0.7. Due to the somewhat low S/N of the spectra and the relatively small sample of RRLs, it may be that the smaller scatter in the difference between $\langle[Fe/H]_{CaT}\rangle$ and $[Fe/H]_{CaT}$ is just due to a stochastic process. However, there are physical indications that would give rise to the scatter being seen, for example, that the largest scatter is when the RRL is at the phase where shocks are strongest, and that the smallest scatter is at phases that have

[10] Heracles likely arose from the Kraken event predicted by Kruijssen et al. (2020), as they both have similar low energies, but a direct connection between Kraken and Heracles has not been established.

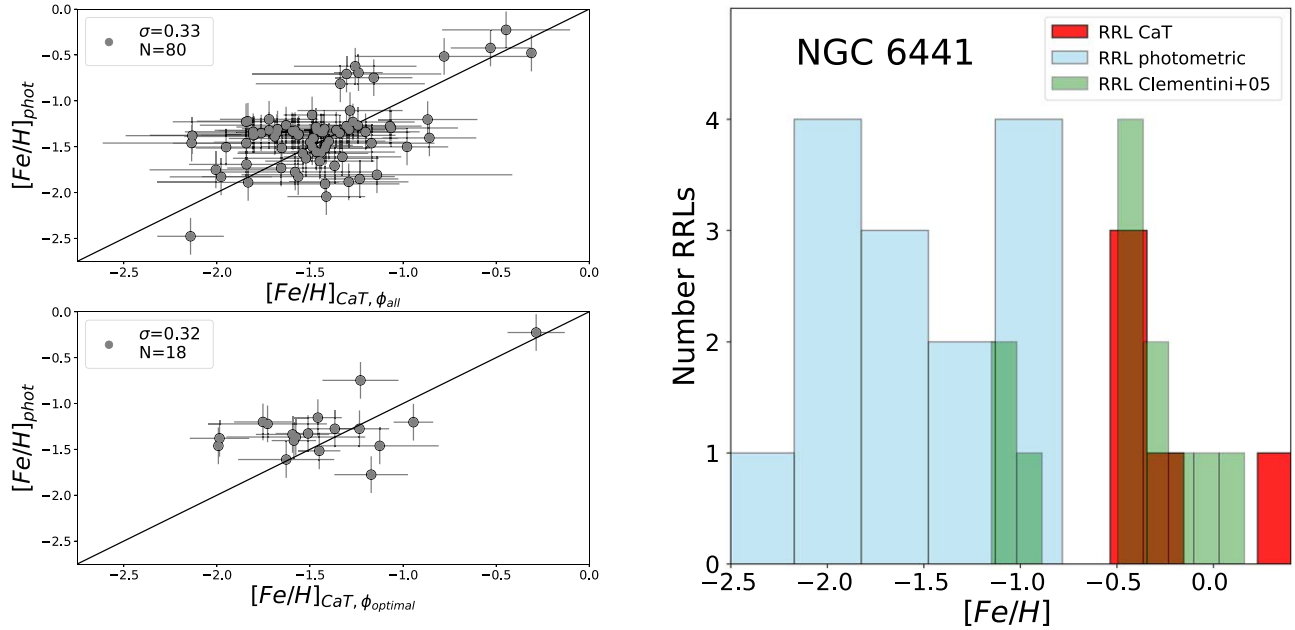

Figure 6. Left: $[Fe/H]_{phot}$ metallicities of Galactic bulge stars as compared to our $[Fe/H]_{CaT}$ metallicities, where $<[Fe/H]_{CaT,\phi_{all}}>$ is the metallicity from individual $[Fe/H]_{CaT}$ measurements averaged over all phases, and $[Fe/H]_{CaT,\phi_{optimal}}$ is where only $[Fe/H]_{CaT}$ at the optimal phases of $\phi = 0.4$–0.5 and $\phi = 0.6$–0.7 are used. Right: the $[Fe/H]$ metallicity distribution of the RRLs in NGC 6441 from $[Fe/H]_{CaT}$, from $[Fe/H]_{phot}$, and from Clementini et al. (2005). Unlike $[Fe/H]_{photo}$, $[Fe/H]_{CaT}$ is also able to reproduce the metallicities of the peculiar, long-period metal-rich RRLs seen in the massive GCs NGC 6441 and NGC 6388.

previously been observed to be a quiescent part of the RRL cycle (e.g., Pancino et al. 2015).

We can obtain $\langle[Fe/H]_{CaT}\rangle$ using observations that fall only between those phases, $\langle[Fe/H]_{CaT}\rangle_{\phi,optimal}$. In this case, there will be fewer $[Fe/H]_{CaT}$ observations to measure a calcium triplet metallicity, but the individual $[Fe/H]_{CaT}$ measurements may be more accurate.

Figure 6 shows how $\langle[Fe/H]_{CaT}\rangle$ and $\langle[Fe/H]_{CaT}\rangle_{\phi,optimal}$ compare to the photometric metallicities, where only stars with three or more $[Fe/H]_{CaT}$ observations are included. For both cases, the correlation between $\langle[Fe/H]_{CaT}\rangle$ and the photometric metallicities gives a similar dispersion, agreeing with the photometric $[Fe/H]$ to within $\sigma = 0.35$. For the case comparing $\langle[Fe/H]_{CaT}\rangle_{\phi,optimal}$ with the photometric metallicities, the bulk of the RRLs have $[Fe/H] \sim -1.5$, and the slope is dominated by one metal-rich RRL.

Of particular interest is how well $[Fe/H]_{CaT}$ metallicities can reproduce the metal-rich RRLs with long periods; such RRLs have to date only been observed in the Galactic bulge, mainly in the massive GCs NGC 6441 and NGC 6388. Photometric metallicities notoriously fail to reproduce the high $[Fe/H]$ metallicities for such long-period RRLs (Clementini et al. 2005). NGC 6441 and NGC 6388 have extended HBs and significant numbers of RRLs with very long periods of ∼0.75 days but are metal-rich (Pritzl et al. 2000, 2001). Metal-rich GCs tend to have very few or no RRLs, and metal-rich RRLs typically have shorter periods compared to their metal-poor counterparts, so the properties of the RRLs in those GCs are surprising, and no satisfactory explanation for the cluster's peculiar RRL population exists.

None of our 83 RRLs are part of the GCs NGC 6441 or NGC 6388, but a handful of stars in the full BRAVA-RR sample do belong to NGC 6441. Five of those stars were observed at optimal phases, and in this way $\langle[Fe/H]_{CaT}\rangle_{\phi,optimal}$ can be calculated. Figure 6 shows the $[Fe/H]_{phot}$ as compared to the medium-resolution spectroscopic metallicities of Clementini et al. (2005) and as compared to our $[Fe/H]_{CaT,\phi_{optimal}}$ metallicities for the GC NGC 6441. Our sample size is small, but the $[Fe/H]_{CaT}$ metallicities are able to recover the metal-rich nature of the NGC 6441 RRLs, in contrast to $[Fe/H]_{phot}$.

We adopt the average $[Fe/H]_{CaT}$ metallicities of all measurements, $\langle[Fe/H]_{CaT}\rangle$, as the metallicity for our Galactic bulge RRL sample. There are 80 RRLs that have between 3 and 12 epochs of observations with S/N >25. In a future paper, we will expand our analysis to also include those BRAVA-RR stars with fewer than eight epochs of observations that happen to have observations taken at optimal phases (such as we did with the RRLs in NGC 6441).

The average metallicities of $\langle[Fe/H]_{phot}\rangle$ and $\langle[Fe/H]_{CaT}\rangle$ of the sample are almost identical at $[Fe/H] \sim -1.4$, with also identical dispersions of $\sigma = 0.36$. This is consistent with what is typically reported in the literature: that photometric metallicities are in agreement with the average metallicity of a population of RRLs, but individual measurements of RRLs may not always be accurate (e.g., Clementini et al. 2023; Dékány et al. 2021).

4.2. Chemodynamics of Galactic Bulge RRLs

To estimate the orbital properties, we used the `galpy`[11] module (Bovy 2015) and implemented the `McMillan17` potential (McMillan 2017) in the aforementioned package. For the Sun's Galactocentric location and rotation velocity, we adopted $R_0 = 8.21$ kpc and $v_0 = 233.1$ km s^{-1}, as specified in the `McMillan17` potential. We utilized values estimated by Schönrich et al. (2010), $(U_\odot, V_\odot, W_\odot) = (11.1, 12.24, 7.25)$. For each RRL, we varied its observed properties within their errors during orbital integration ($t = 2$ Gyr) and estimated the average orbital properties (e.g., angular momentum L_z and orbital energy E_{tot}) along with their dispersion.

[11] https://docs.galpy.org/en/v1.9.2/

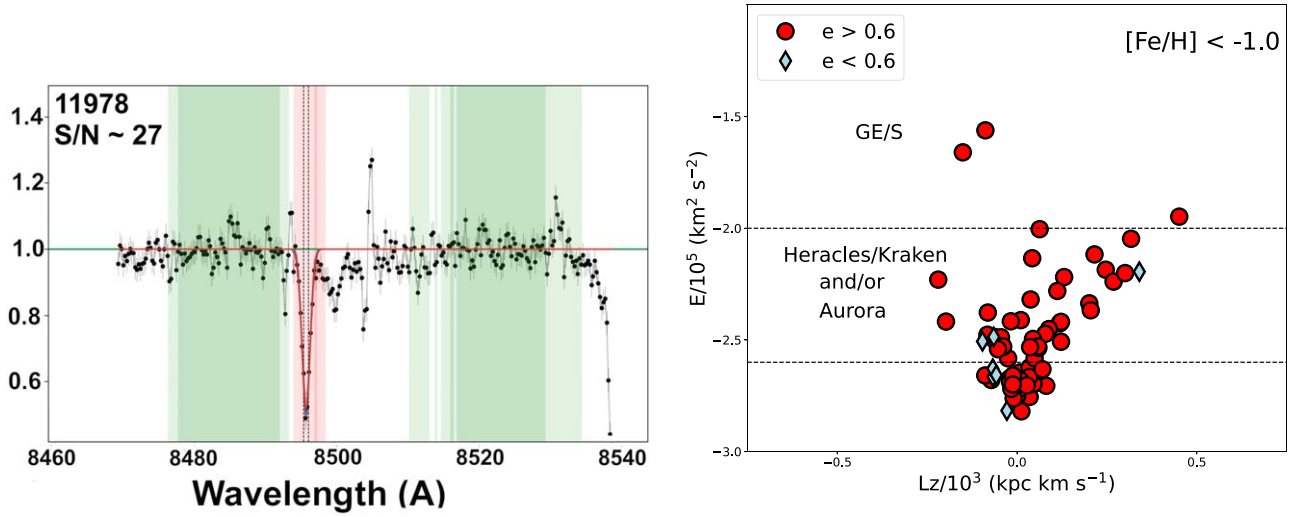

Figure 7. Left: a typical BRAVA-RR spectrum used for $[Fe/H]_{CaT}$ abundance determination from the measured EW of the CaT line at 8498 Å. Right: the total energy (E_{tot}) vs. the z component of the angular momentum (L_z) for the Galactic bulge RRLs studied here. Stars belonging to the same physical structure cluster together in integrals of motion such as E_{tot} and angular momentum, and the major substructure of GE/S is labeled. The E_{tot} and angular momentum regime where Aurora is seen is also where the potential Heracles/Kraken substructure is thought to reside.

Figure 7 (right panel) shows the (L_z, E) orbit distribution of the RRLs with metallicities more metal-poor than $[Fe/H]_{CaT} < -1.0$. The stellar orbit distribution depends mainly on the metallicity and radial distance of the stars probed. Probing small radial distances from the Galactic center gives the possibility to detect stars with the lowest energies. The Galactic disk and the in situ populations will dominate at $[Fe/H] > -1.0$, and the halo and possible accreted populations will become apparent at $[Fe/H] < -1.0$. Simulations of MW-like galaxies indicate that mergers contribute to a small fraction of the stellar component, and so the majority of stars with low metallicities and energies will belong to the in situ component of the MW (e.g., Gargiulo et al. 2019; Semenov et al. 2024). In an attempt to uncover accreted structures, Mg, Mn, Al, and Fe abundances (e.g., Hawkins et al. 2015; Das et al. 2020; Naidu et al. 2020) are often used. Using these elemental abundances, primarily [Al/Fe], it has also been put forward that almost all stars in the inner Galaxy with $[Fe/H] < -1.0$ and low energies formed in situ in what has been dubbed Aurora (Belokurov & Kravtsov 2022). This is because stars at low metallicities and low energies consistently have higher [Al/Fe] ratios as compared to the same stars at higher energies, whereas accreted stars would be depleted in [Al/Fe]. However, using similar diagnostics, it has also been put forward that stars at low energies and metallicities can belong to a massive system that merged early in the history of the MW, the Kraken/Heracles (Kruijssen et al. 2020; Horta et al. 2021). It is still not clear whether Heracles/Kraken is in fact a separate accreted component in the MW or whether Aurora contains most or all of the alleged Kraken/Heracles structure.

In Figure 7, two RRLs are consistent with belonging to the low-metallicity substructure discussed in the introduction, GE/S. A striking 58% of our sample consists of RRLs consistent with Heracles/Kraken, as they have highly eccentric orbits and energies between -2×10^5 km^2 s^{-2} and -2.6×10^5 km^2 s^{-2}. Due to the $[Fe/H]_{CaT}$ uncertainties, there may be a few metal-rich contaminants that ended up in this sample, but given the paucity of metal-rich RRLs (see, e.g., left panel of Figure 6), this should be a small number and would not affect our conclusions. This energy regime also overlaps with the in situ Aurora regime. The high fraction of RRLs found with these energies is not compatible with these RRLs belonging to an accreted component alone—accreted components will not dominate in the inner Galaxy—and therefore we interpret the low-energy RRLs as belonging mainly to the in situ Aurora bulge. It may be that there is some contamination from accretion, but with the absence of elemental abundances for these RRLs, it is difficult to make firm conclusions.

5. Conclusions

Here 68 spectra from a sample of 40 RRLs with metallicities derived from Fe(II) and Fe(I) abundances are used to verify the correlation between [Fe/H] and the EW of the Ca ii line at 8498 Å for RRLs. The correlation we obtain is almost identical to that obtained by Wallerstein et al. (2012), but our relation has associated uncertainties, which allows error estimations on our derived $[Fe/H]_{CaT}$ metallicities. Our $[Fe/H]_{CaT}$ metallicities are a factor of 2 more precise than the Gaia photometric metallicities released in DR3 (Clementini et al. 2023), and our metallicities are especially accurate for spectra with $S/N > 35$. We publicly release 175 spectroscopic metallicities for the Gaia RRLs with RVS spectra available to the community. This number will increase dramatically for the next Gaia releases. Our analysis suggests that the average $[Fe/H]_{CaT}$ measurement, $\langle[Fe/H]_{CaT}\rangle$, is a good reference for the metallicity of an RRL, and this will especially hold when the spectra evenly cover the whole pulsation cycle. Given the Gaia scanning law, this will be the case for most of the Gaia RRL sample.

We show that photometric metallicities are influenced by their [α/Fe], in a sense that $[Fe/H]_{phot}$ appears to be more depleted in [Fe/H] for RRLs with lower [α/Fe] ratios. This bias is not observed, or at least is not as strong, for metallicities derived from the EW of CaT. We further show that $[Fe/H]_{CaT}$ correctly recovers the high [Fe/H] abundances observed in the long-period metal-rich population of RRLs in NGC 6441. This has been a challenge for photometric metallicity relationships.

Using a sample of 80 RRLs with more than eight epochs of observations in the BRAVA-RR survey, we find a small

number of RRLs with properties consistent with belonging to the accreted GE/S substructure. We find a much larger number of RRLs consistent with having high eccentricities, having low energies, and being without a prominent rotating component, which are properties of Kraken/Heracles. Due to the large fraction (>50%) of the RRL population inhabiting such a low-energy regime, these stars were likely not accreted, but they are part of the in situ MW stellar population that formed before the Galaxy had a coherently rotating disk, Aurora. The commanding presence of RRLs with properties consistent with Aurora, much more so than, e.g., the RRLs with properties of the GE/S, is in agreement with Aurora being formed sufficiently early, before any coherent disk is established.

The relationship between the EW of the CaT and [Fe/H] allows one of the fundamental properties, [Fe/H], of RRLs to be derived for stars at the distance of the Galactic bulge and beyond, as well as for the thousands of RRLs observed with Gaia RVS. We will apply our relationship to a wider sample of BRAVA-RR stars, as well as to those with fewer than eight epochs, and to Gaia RRLs observed with RVS and released in the upcoming DR4.

Acknowledgments

A.M.K. acknowledges support from grant AST-2009836 from the National Science Foundation. A.M.K., C.S., K.R.C., J.H., and K.D. acknowledge the M. J. Murdock Charitable Trust's support through its Research Across Institutions for Scientific Empowerment (RAISE) program. This work was made possible through the Preparing for Astrophysics with LSST Program, supported by the Heising-Simons Foundation and managed by Las Cumbres Observatory. This research was supported by the Munich Institute for Astro-, Particle and BioPhysics (MIAPbP), which is funded by the Deutsche Forschungsgemeinschaft (DFG, German Research Foundation) under Germany's Excellence Strategy - EXC-2094 - 390783311.

This work has made use of data from the European Space Agency (ESA) mission Gaia (https://www.cosmos.esa.int/gaia), processed by the Gaia Data Processing and Analysis Consortium (DPAC, https://www.cosmos.esa.int/web/gaia/dpac/consortium). Funding for the DPAC has been provided by national institutions, in particular the institutions participating in the Gaia Multilateral Agreement.

Appendix
Photometric Metallicities

A number of different photometric metallicity relations based on the Gaia *G*-band photometry have been put forward. To date, none of these use the Crestani et al. (2021a) sample of RRLs as a calibrating sample. We believe that this sample is superior in terms of its number of RRLs, wide metallicity baseline, high spectral resolution, and homogeneity of the analysis, and here we recalibrate period−metallicity (PM) relations to estimate photometric metallicities using the publicly available photometric data provided in the Gaia RRL catalog (Clementini et al. 2023). Our approach is similar to our previous study in which we calibrate absolute magnitudes of RRLs from the Gaia RRL parallaxes (see Sections 2 and 3 in Prudil et al. 2024a). Briefly, spectroscopic metallicities are collected from Crestani et al. (2021a, 2021b) and Dékány et al. (2021) and matched with the corresponding star from the Gaia RRL catalog. Our data set is then divided into two groups based on the pulsation mode, and stars not fulfilling the following criteria are discarded:

$$\mathrm{RUWE} < 1.4 \quad \text{and} \quad \texttt{ipd\_frac\_multi\_peak} < 5. \tag{A1}$$

This results in 20 RRc and 155 RRab calibration variables. In our fitting procedure, we optimize the following expression for predicting photometric metallicities:

$$[\mathrm{Fe/H}]_{\mathrm{phot}} = \alpha P + \beta\varphi_{31} + \gamma, \tag{A2}$$

where P and φ_{31} represent pulsation periods and phase differences between two Fourier coefficients, respectively, and α, β, and γ stand for parameters of the fit. As an additional parameter characterizing the intrinsic scatter in the photometric metallicity relation, we used $\varepsilon_{[\mathrm{Fe/H}]}$. In the optimization procedure, we follow the described procedure in Prudil et al. (2024a), but we minimized the difference between spectroscopic metallicities from the literature and those predicted from Equation (A2). The results of our calibration are depicted in Figure 8 and summarized by the following equations, where N denotes the total number of RRL variables used in calibration:

$$[\mathrm{Fe/H}]^{\mathrm{RRab}}_{\mathrm{phot}} = -5.5061\,P + 0.8143\,\varphi_{31} - 0.0813, \quad N = 155 \tag{A3}$$

$$[\mathrm{Fe/H}]^{\mathrm{RRc}}_{\mathrm{phot}} = -13.2023\,P + 0.5138\,\varphi_{31} + 0.7338, \quad N = 20. \tag{A4}$$

The covariance matrices for both relations with associated intrinsic scatters are the following:

$$\mathrm{Cov}_{K_s} = \begin{bmatrix} \sigma_{\alpha_{\mathrm{RRab}}} & \sigma_{\beta_{\mathrm{RRab}}} & \sigma_{\gamma_{\mathrm{RRab}}} \\ 0.019144 & -0.001096 & -0.008282 \\ -0.001096 & 0.000928 & -0.001310 \\ -0.008282 & -0.001310 & 0.007427 \end{bmatrix} \quad \varepsilon_{[\mathrm{Fe/H}]_{\mathrm{RRab}}} = 0.247 \tag{A5}$$

$$\mathrm{Cov}_{\mathrm{RRc}} = \begin{bmatrix} \sigma_{\alpha_{\mathrm{RRc}}} & \sigma_{\beta_{\mathrm{RRc}}} & \sigma_{\gamma_{\mathrm{RRc}}} \\ 0.758431 & -0.011111 & -0.185556 \\ -0.011111 & 0.003445 & -0.008078 \\ -0.185556 & -0.008078 & 0.082015 \end{bmatrix} \quad \varepsilon_{[\mathrm{Fe/H}]_{\mathrm{RRc}}} = 0.193. \tag{A6}$$

Figure 8 shows the best-fit relations. The metallicity interval has a sufficient number of metal-rich ([Fe/H] > −0.5) and metal-poor ([Fe/H] < −2.0) RRLs, especially for the RRab stars (left panel). A moderate systematic trend of the residuals for the metal-rich end is seen, where our photometric metallicity relation tends to underestimate the metallicity. One reason for this is that the [α/Fe] of an RRL also influences the shape of its light curve, and metal-rich RRLs tend to also be depleted in [α/Fe], unlike the more metal-poor RRLs.

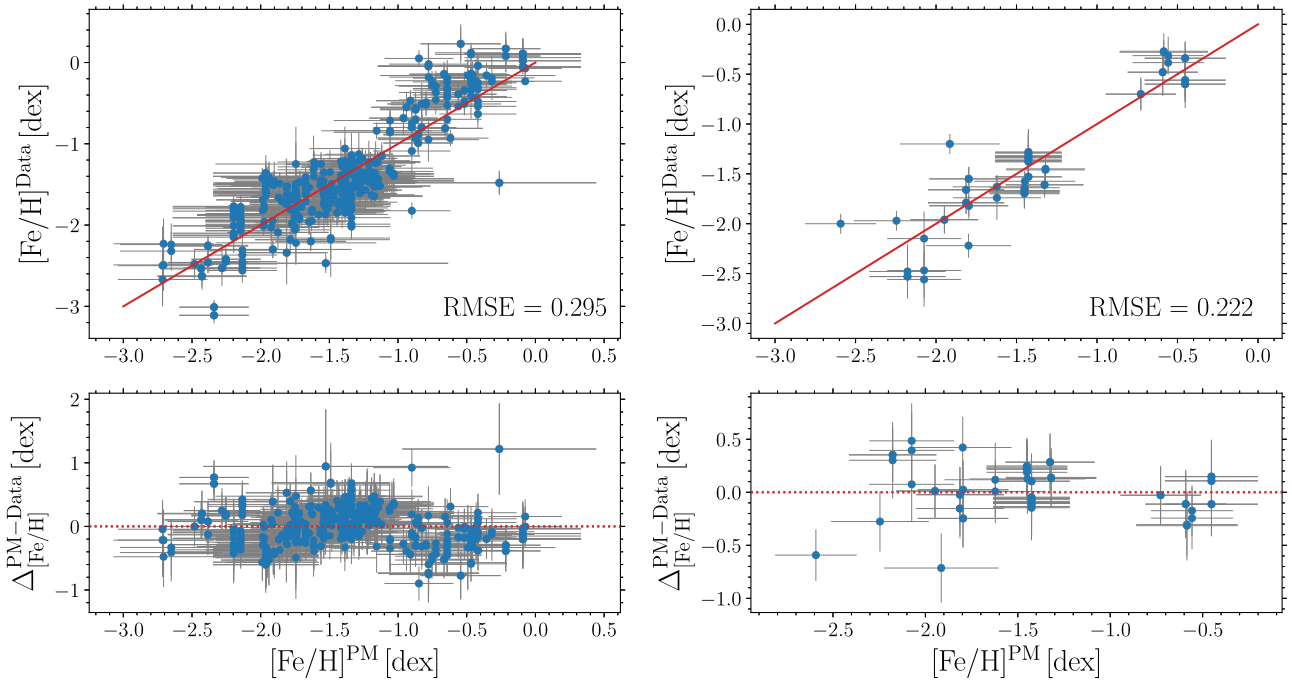

Figure 8. Comparison of the photometric metallicities predicted from newly derived PM relations for RRab (left) and RRc (right) in this study based on Gaia *G*-band photometry.

ORCID iDs

Andrea Kunder https://orcid.org/0000-0002-2808-1370
Zdenek Prudil https://orcid.org/0000-0001-5497-5805
Claire Skaggs https://orcid.org/0009-0009-4825-429X
Henrique Reggiani https://orcid.org/0000-0001-5761-6779
David M. Nataf https://orcid.org/0000-0001-5825-4431
Joanne Hughes https://orcid.org/0000-0002-9074-0306
Kevin R. Covey https://orcid.org/0000-0001-6914-7797
Kathryn Devine https://orcid.org/0000-0002-3723-6362

References

Ardern-Arentsen, A., Monari, G., Queiroz, A. B. A., et al. 2024, MNRAS, 530, 3391
Armandroff, T. E., & Zinn, R. 1988, AJ, 96, 92
Belokurov, V., Erkal, D., Evans, N. W., Koposov, S. E., & Deason, A. J. 2018, MNRAS, 478, 611
Belokurov, V., & Kravtsov, A. 2022, MNRAS, 514, 689
Belokurov, V., Sanders, J. L., & Fattahi, A. 2020, MNRAS, 494, 3880
Blanco, B., & Blanco, B. 1984, MmSAI, 56, 15
Blanco-Cuaresma 2019, MNRAS, 486, 2075
Blanco-Cuaresma, S., Soubiran, C., Heiter, U., & Jofré, P. 2014, A&A, 569, 111
Bono, G., Caputo, F., Castellani, V., et al. 2003, MNRAS, 344, 1097
Bovy, J. 2015, ApJS, 216, 29
Butler, D. 1975, ApJ, 200, 68
Butler, D., Manduca, A., Deming, D., & Bell, R. A. 1982, AJ, 87, 640
Butler, E., Kunder, A., Prudil, Z., et al. 2024, ApJL, 963, L33
Cacciari, C., Clementini, G., & Femley, J. A. 1992, ApJ, 396, 219
Carney, B. W., Storm, J., & Jones, R. V. 1992, ApJ, 386, 663
Carrera, R., Pancino, E., Gallart, C., & del Pino, A. 2013, MNRAS, 434, 1681
Catelan, M., Pritzl, B. J., & Smith, H. A. 2004, ApJS, 154, 633
Chadid, M., Sneden, C., & Preston, G. W. 2017, ApJ, 835, 187
Christy, R. F. 1966, ApJ, 144, 108
Clementini, G., Gratton, R. G., & Bragaglia, A. 2005, ApJ, 630, 145
Clementini, G., Ripepi, V., Garofalo, A., et al. 2023, A&A, 674, 18
Clementini, G., Tosi, M., & Merighi, R. 1991, AJ, 101, 2168
Cook, B. T., Woods, D. F., Ruprecht, J. D., et al. 2022, MNRAS, 513, 2509
Crestani, J., Braga, V. F., Fabrizio, M., et al. 2021a, ApJ, 914, 10
Crestani, J., Fabrizio, M., Braga, V. F., et al. 2021b, ApJ, 908, 20
Dall'Ora, M., Storm, J., Bono, G., et al. 2004, ApJ, 610, 269
Dambis, A. K., Berdnikov, L. N., & Kniazev, A. Y. 2013, MNRAS, 435, 3206
Das, P., Hawkins, K., Jofré, P., et al. 2020, MNRAS, 493, 5195
Dékány, I., & Grebel, E. K. 2022, ApJS, 261, 33
Dékány, I., Grebel, E. K., & Pojma'nski, G. 2021, ApJ, 920, 33
Demarque, P., Zinn, R., Lee, Y. W., & Sukyoung, Y. 2000, AJ, 119, 1398
Fabrizio, M., Bono, G., Braga, V. F., et al. 2019, ApJ, 882, 169
Feng, Y., Guhathakurta, P., Peng, E., et al. 2024, ApJ, 966, 159
Fernley, J. A. 1993, A&A, 268, 591
Fernley, J., Barnes, T. G., Skillen, I., et al. 1998, A&A, 330, 515
For, B.-Q., Sneden, C., & Preston, G. W. 2011, ApJS, 197, 29
Foreman-Mackey, D., Hogg, D. W., Lang, D., & Goodman, J. 2013, PASP, 125, 306
Gaia Collaboration, Vallenari, A., et al. 2023a, A&A, 674, A1
Gargiulo, I. D., Monachesi, A., & Gómez, F. A. 2019, MNRAS, 489, 5742
Gilligan, C., Chaboyer, B., Marengo, M., et al. 2021, MNRAS, 503, 4719
Hawkins, K., Jofré, P., Masseron, T., & Gilmore, G. 2015, MNRAS, 453, 758
Helmi, A., Babusiaux, C., Koppelman, H. H., et al. 2018, Natur, 563, 85
Hogg, D. W., Bovy, J., & Lang, D. 2010, arXiv:1008.4686
Horta, D., Schiavon, R. P., Mackereth, J. T., et al. 2021, MNRAS, 500, 1385
Iorio, G., & Belokurov, V. 2021, MNRAS, 502, 5686
Jurcsik, J., & Hajdu, G. 2023, MNRAS, 525, 3486
Jurcsik, J., & Kovacs, G. 1996, A&A, 312, 111
Kanbur, S. M., & Mariani, H. 2004, MNRAS, 355, 1361
Kolenberg, K., Fossati, L., Shulyak, D., et al. 2010, A&A, 519, A64
Kruijssen, J. M. D., Pfeffer, J. L., Chevance, M., et al. 2020, MNRAS, 498, 2472
Kunder, A., Pérez-Villegas, A., Rich, R. M., et al. 2020, AJ, 159, 270
Kunder, A., Rich, R. M., Koch, A., et al. 2016, ApJL, 821, L25
Layden, A. C. 1994, AJ, 108, 1016
Li, X.-Y., Huang, Y., Liu, G.-C., Beers, T. C., & Zhang, H.-W. 2023, ApJ, 944, 88
Liu, G. C., Huang, Y., Zhang, H. W., et al. 2020, ApJS, 247, 68
Liu, S., Zhao, G., Chen, Y.-Q., Takeda, Y., & Honda, S. 2013, RAA, 13, 1307
Liu, T. 1991, PASP, 103, 205
Liu, T., & Janes, K. A. 1990, ApJ, 354, 273
Longmore, A. J., Fernley, J. A., & Jameson, R. F. 1986, MNRAS, 220, 279
Madore, B. F., & Freedman, W. L. 2012, ApJ, 744, 132
Marconi, M., Coppola, G., Bono, G., et al. 2015, ApJ, 808, 50
Massari, D., Koppelman, H. H., & Helmi, A. 2019, A&A, 630, 4
Matijevič, G., Chiappini, C., Grebel, E. K., et al. 2017, A&A, 603, 19
McMillan, P. J. 2017, MNRAS, 465, 76
McNamara, D. H. 1997, PASP, 109, 857
Medina, G. E., Muñoz, R., Carlin, J. L., Vivas, A. K., et al. 2024, MNRAS, 531, 4762

Muhie, T. D., Dambis, A. K., Berdnikov, L. N., Kniazev, A. Y., & Grebel, E. K. 2021, MNRAS, 502, 4074
Mullen, J. P., Marengo, M., Martínez-Vázquez, C. E., et al. 2021, ApJ, 912, 144
Muraveva, T., Delgado, H. E., Clementini, G., Sarro, L. M., & Garofalo, A. 2018, MNRAS, 481, 1195
Naidu, R. P., Conroy, C., Bonaca, A., et al. 2020, ApJ, 901, 48
Neeley, J. R., Massimo, M., Freedman, W. L., et al. 2019, MNRAS, 490, 4254
Nemec, J. M., Cohen, J. G., & Ripepi, V. 2013, ApJ, 773, 181
Pancino, E., Britavskiy, N., Romano, D., et al. 2015, MNRAS, 447, 2404
Preston, G. W. 1959, ApJ, 130, 507
Preston, G. W., Sneden, C., & Chadid, M. 2022, AJ, 109, 163
Pritzl, B., Smith, H. A., Catelan, M., & Sweigart, A. V. 2000, ApJ, 530, 41
Pritzl, B., Smith, H. A., Catelan, M., & Sweigart, A. V. 2001, AJ, 122, 2600
Prudil, Z., Dékány, I., Catelan, M., et al. 2019, MNRAS, 484, 4833
Prudil, Z., Dékány, I., Grebel, E. K., & Kunder, A. 2020, MNRAS, 492, 3408
Prudil, Z., Hanke, M., Lemasle, B., et al. 2021, A&A, 648, 78
Prudil, Z., Kunder, A., Dékány, I., & Koch-Hansen, A. J. 2024a, A&A, 684, 176
Prudil, Z., Smolec, R., Kunder, A., Koch-Hansen, A. J., & Dékány, I. 2024b, A&A, 685, 153
Queiroz, A. B. A., Chiappini, C., Perez-Villegas, A., et al. 2021, A&A, 656, 156
Sandage, A. 1993, AJ, 106, 703
Savino, A., Koch, A., Prudil, Z., Kunder, A., & Smolec, R. 2020, A&A, 641, 96
Schönrich, R., Binney, J., & Dehnen, W. 2010, MNRAS, 403, 1829
Semenov, V. A., Conroy, C., Chandra, V., Hernquist, L., & Nelson, D. 2024, ApJ, 962, 84
Sesar, B., Hernitschek, N., Dierickx, M. I., Fardal, M. A., & Rix, H.-W. 2017, ApJL, 844, 4
Sneden, C., Preston, G. W., Chadid, M., & Adamów, M. 2017, ApJ, 848, 68
Starkenburg, E., Hill, V., Tolstoy, E., et al. 2010, A&A, 513, A34
Steinmetz, M., Matijeviĉ, G., Enke, H., et al. 2020, AJ, 160, 82
Sweigart, A. V., & Gross, P. G. 1978, ApJS, 35, 405
Vivas, A. K., Saha, A., Olsen, K., et al. 2017, AJ, 154, 85
Wallerstein, G., Gomez, T., & Huang, W. 2012, Ap&SS, 341, 89
Walker, A. R., & Terndrup, D. M. 1991, ApJ, 378, 119